ADVANCED FUNCTIONAL MATERIALS
www.afm-journal.de

Harnessing Berthollide Configuration Entropy for Expedited K^+ Storages

*Kai-Siang Jhang, Yi-Chun Yang, Ying-Rui Lu, Kai-Yuan Hsiao, Ming-Yen Lu, and Hsing-Yu Tuan**

Variations in configurational entropy greatly influence the electrochemical behavior of materials; those featuring expanded surface areas, numerous active sites, and accelerated reaction kinetics are highly valued for their superior electrocatalytic properties. In this study, a Berthollide compound is introduced, designated as $Cu_3Sb_{0.93}Bi_{0.06}Sn_{0.01}S_2Se_2$ (C(ABT)(SSe)). This material, cations, and anions co-doped Cu_3SbS_4 (CAS), exhibit significantly enhanced storage performance in potassium-ion batteries (PIBs). The introduction of foreign elements improved conductivity, while dual-site conversion and alloying elements enhanced ion diffusion, charge transfer, and electrode kinetics. Regulating configurational entropy created more active sites for Sb. Using high-capacity Sb and S as primary components, material's configurational entropy is precisely adjusted through active element doping, forming a non-stoichiometric structure with thermodynamically stable defect active sites. The synergistic effect of trivalent active metals, particularly high-valence Sb^{5+}, demonstrated superior electrochemical performance compared to materials with unregulated entropy values. Compared to CAS, with the increase in configurational entropy to 0.975 R, the K^+ diffusion energy is reduced by 40% and increasing electronic conductivity by 2.6 times, boosting high rate performance (10 A g^{-1}), and showing 49.5% higher capacity after 700 cycles. This novel entropy regulation strategy offers new insights into the design of multi-element configurational entropy PIBs.

1. Introduction

Potassium-ion batteries (PIBs) share similar physical and chemical properties with lithium-ion batteries, including high energy density due to the low standard reduction potential of K^+/K (−2.93 V vs standard hydrogen electrodes), close to that of Li^+/Li (−3.04 V).[1–4] Potassium is abundant and cost-effective, and the weak Lewis acidity of K^+ produces the smallest Stokes radius among organic solvents (K^+: 3.6 Å), facilitating ionic diffusivity. These batteries operate via three electrochemical mechanisms: insertion, conversion, and alloying.[5–11] Incorporating alloy in reactions using elements like P, Sn, Bi, and Sb or conversion reactions elements like S, Se, and Te in the anode material is crucial for boosting capacity and electrochemical performance.[12–16] Anodes that utilize the alloying mechanism offer high energy density and low operating potential.[17–23] For optimal electrochemical performance, these elements must be integrated into the compounds. Particularly, Sb and S enhance reaction performance significantly due to their high conductivity and capacity.[24–29]

Berthollides are non-stoichiometric compounds, solid materials that deviate from the law of definite proportions, exemplified by $Li_{1+x}Ni_{1-x}O_2$ or $Cu_{2-x}Se$.[30,31] By employing heteroatom doping, vacancy engineering, defect engineering, and entropy tuning, Berthollides achieve composition ratios not confined to small integer values.[32–37] While their compositions vary, their phases and space groups typically align with those of their stoichiometric counterparts. These compounds form when defects alter the stoichiometry of known chemically stable structures. Generally, four types of defects arise in non-stoichiometric compounds, including anion vacancies/interstitials and cation vacancies/interstitials.[38] Berthollides achieve compositions beyond small integer values through impurity doping, vacancy engineering, and defect engineering. These modifications can adjust material properties including 1) Electronic structure, 2) Coordination environment, 3) Structural stability, 4) Electronic conductivity enhancement, and 5) Ion diffusion. Thermodynamically, Berthollides often lead to an increase in the system's free energy as they may be in an unstable state. This deviation can be balanced through chemical reactions to achieve a more stable state. These advancements in material modification are pivotal for improving performance and broadening the applications of electrochemical systems in energy storage systems.

K.-S. Jhang, Y.-C. Yang, H.-Y. Tuan
Department of Chemical Engineering
National Tsing Hua University
Hsinchu 30013, Taiwan
E-mail: hytuan@che.nthu.edu.tw
Y.-R. Lu
National Synchrotron Radiation Research Center
Hsinchu 300, Taiwan
K.-Y. Hsiao, M.-Y. Lu
Department of Materials Science and Engineering
National Tsing Hua University
Hsinchu 30013, Taiwan

The ORCID identification number(s) for the author(s) of this article can be found under https://doi.org/10.1002/adfm.202411082

DOI: 10.1002/adfm.202411082

For instance: Cheng et al. demonstrated that $Li_{1+x}Ni_{1-x}O_2$ exhibits significantly better performance because of Li-refeeding modification for nonstoichiometric Ni-rich cathode materials, compared to near-stoichiometric $LiNiO_2$. Huang et al. synthesized the different crystal structures of Cu_xSe by adjusting the stoichiometry in a zinc-ion battery. Cubic $Cu_{2-x}Se$ demonstrates superior stability, better conductivity, and lower Zn^{2+} diffusion barriers than the hexagonal CuSe electrode. The non-stoichiometric strategy offers numerous advantages in energy storage. However, to generate vacancies at the Sb sites, expose more active sites, and promote the effective formation of Berthollides, it is crucial to selectively dope trace amounts of active potassium ions and choose appropriate doping elements.

Increasing configurational entropy through cation or anion mixing to form Berthollides helps promote chemical and structural diversity. According to reports, Fei et al. designed $Cu_4MnFeSnGeS_8$ based on Cu_3SnS_4 by mixing different transition metals.[38] This entropy-driven sodium-ion battery anode effectively prevents continuous SEI film breakage and electrode pulverization, enabling highly reversible conversion reactions. However, entropy-regulated materials containing transition metals may exhibit reduced overall capacity due to the high proportion of transition metals, which are unreactive with potassium ions.[39] Therefore, developing entropy-regulated anode with high reactivity becomes crucial. Additionally, entropy regulation, with its multi-element synergistic effects, allows for a multi-site entropy regulation strategy to comprehensively improve the shuttle effect and volumetric expansion that occur during the coexistence of conversion-type and alloy-type reactions, thereby preventing capacity degradation and ensuring stable cycling performance.[40–43] In PIBs, both conversion and alloy-type reactions are equally important. Due to the multi-element composition and the complex incorporation of cations and anions with different physical and chemical properties, the presence of various ions leads to different chemical environments.[44] Thus, investigating how increased configurational entropy affects the chemical environment to enhance energy storage efficiency remains a subject for further study.[35,45–47]

Here, we design a non-stoichiometric compound with multiple reactive elements that includes highly conductive copper to ensure high conductivity, high-capacity sulfur group elements, and alloy-type group VA elements. Based on the Cu_3SbS_4 (CAS) structure, $Cu_3Sb_{0.93}Bi_{0.06}Sn_{0.01}S_2Se_2$ (C(ABT)(SSe)) can be tuned from 0 R to 0.975 R through cation/anion co-doping. Due to configuration entropy adjustment, the conductivity, energy band structure, and ionic diffusion and energy barriers of CAS can be further modulated. Bi and Sn metals are optimal for enhancing the capacity of PIBs due to their compatibility with the K-ion, in contrast to the inertness of As. Se doping catalyzes thermodynamic conversion reactions and has similar physical and chemical properties to S, used in the synthesis of $Cu_3SbS_2Se_2$ (CA(SSe)). Doping Bi and Sn into the Sb site of the CA(SSe), known for its low operational potential, cost-effectiveness, and high theoretical capacity, makes it a prime candidate for an entropy-regulated Berthollides host material. Compared to CAS, C(ABT)(SSe) exhibited a 49.5% increase in capacity after 700 cycles, nearly a 70% capacity in rate performance (1 A g^{-1}), and 206.9% lower discharge overpotential at 200 mA g^{-1}. The DFT results at the doping sites reveal a 40% reduction in diffusion energy. The C(ABT)(SSe)||PB full cells has 33.6% higher capacity at 3 A g^{-1}. This study provides the design strategy—strategically cation/anion tuning and entropy adjustment—advancing the development of high-performance PIBs with improved efficiency and stability.

2. Results and Discussion

2.1. Design of Non-Stoichiometric Entropy Tuning

According to the Hume-Rothery Rules, the difference in atomic radii between solute and solvent atoms should be less than 15%, calculated using the formula: % difference = ((radius of solute – radius of solvent)/radius of solvent) × 100.[48] Additionally, for elemental monomers, the solute and solvent atoms must have similar electronegativities to avoid forming intermetallic compounds and instead form solid solutions. For anion doping, the electronegativities of sulfur (S) and selenium (Se) are 2.58 and 2.55, respectively, with a radius difference of 3%. Due to the high capacity and high stability advantages of S and Se, a $Cu_3SbS_2Se_2$ solid solution was synthesized, aiming to achieve a synergistic effect in electrochemical performance. For cation doping at the Sb site, the electronegativities of Sb, Bi, and Sn are set at 2.05, 2.02, and 1.96, respectively, indicating their closely matched values and strong chemical compatibility. Utilizing Sb as the base solvent, the radius differences for doped Bi and Sn are 10.34% and 0% respectively, highlighting the excellent chemical compatibility of entropy-adjusted C(ABT)(SSe). To calculate the material entropy, we employ the equation $\Delta S = -R\sum ni\ x|\ lnx\ |$, where R represents the ideal gas constant, and xi denotes the mole fraction occupied by the elemental site (**Figure 1a**).[49] Anionic doping adjusts the material entropy of CAS to 0.693R. As a result, solid solutions form where Sb is adjacent to S and Se, creating defective vacancies and more active sites. Simulation calculations show that the thermodynamic potential for defect formation in Sb sites of CA(SSe) (1.14 eV) is lower than in non-entropy-adjusted CAS (1.89 eV) and Cu_3SbSe_4 (CASe) (2.09 eV), indicating a greater likelihood of defect migration to active sites and the benefits of substituting S with Se for enhanced chemical stability against anionic doping (Figure 1b). This strategy harnesses the advantages of S and Se in PIBs and incorporates a dual cation doping approach at the Sb site to further modulate material entropy. By introducing Bi and Sn, the entropy value is raised to 0.975 R, allowing adjustments to the physical and chemical properties while maintaining structural stability. The simulation results indicate a lower thermodynamic potential for Sb defect formation (1.01 eV), suggesting that the increase in configurational entropy significantly aids in stabilizing the formation energy of active sites (Figure 1c). Consequently, this method enhances the chemical reactivity of the material. Moreover, the finding from the charge density difference diagram reveals a greater accumulation of charge at the Sb sites in C(ABT)(SSe) compared to CA(SSe), CAS, and CASe without cation doping, indicating enhanced charge distribution and alloying reactions due to entropy adjustment with Bi and Sn (Figure 1d; Figures S1–S3, Supporting Information). Additionally, the total density of states (TDOS) for C(ABT)(SSe) is

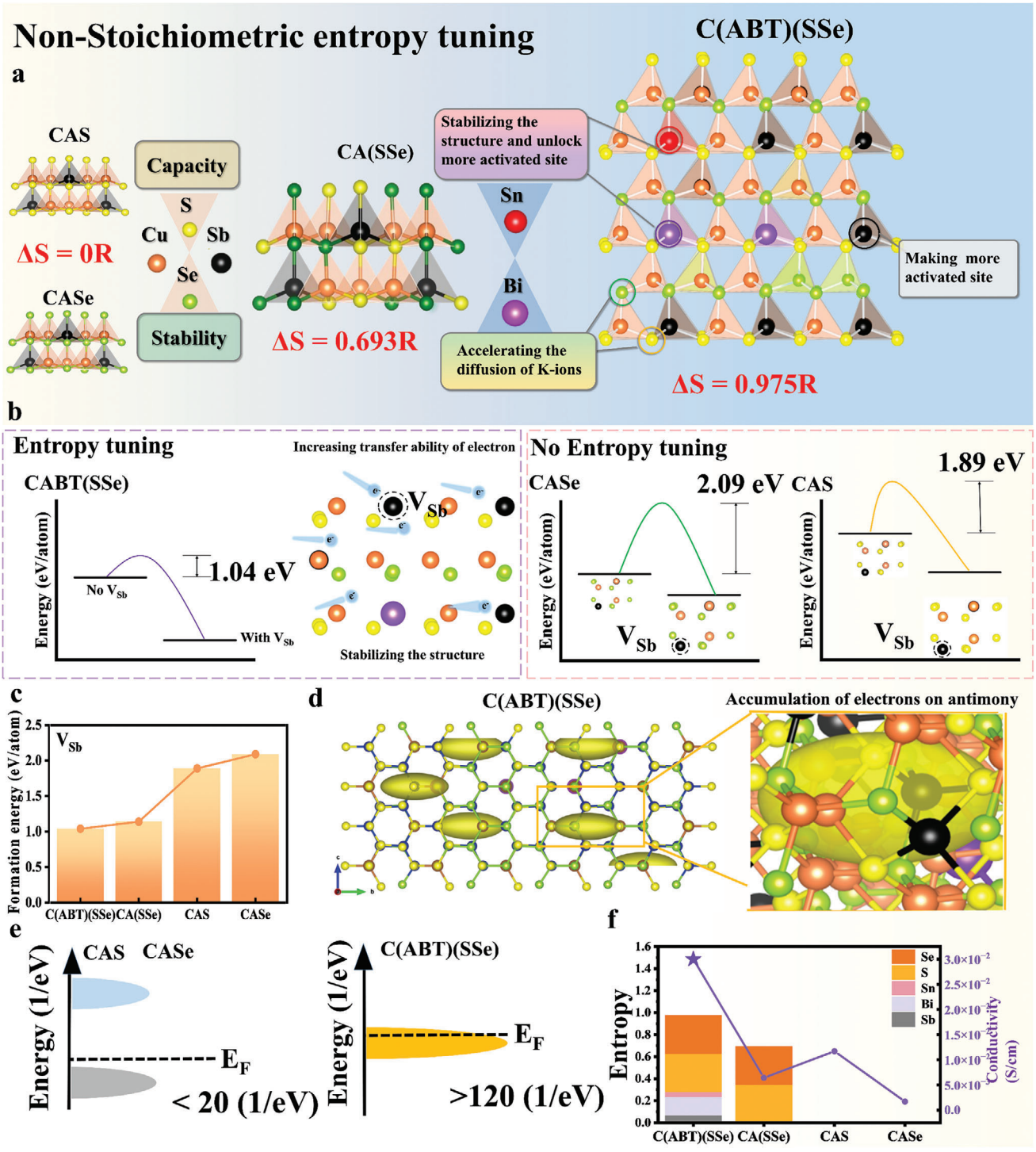

Figure 1. a) Entropy evolution of C(ABT)(SSe). b,c) Vacancy formation energy of Sb site. d) Charge density difference of C(ABT)(SSe). e) TDOS of different entropy materials. f) The relationship between entropy and conductivity.

significantly more than six times higher than that of CAS and CASe, demonstrating the substantial impact of anion addition on the material's density of states (Figure 1e). As a result, conductivity measurements show an increase from 6.4×10^{-3} to 30×10^{-3} S cm^{-1} upon doping Bi and Sn at the Sb site, enhancing electron transfer for faster charging and discharging, and thus more efficient battery operation (Figure 1f). Additionally, doping with trace non-stoichiometric cations increases the entropy value, improving material disorder and electrochemical reactivity of anode materials.

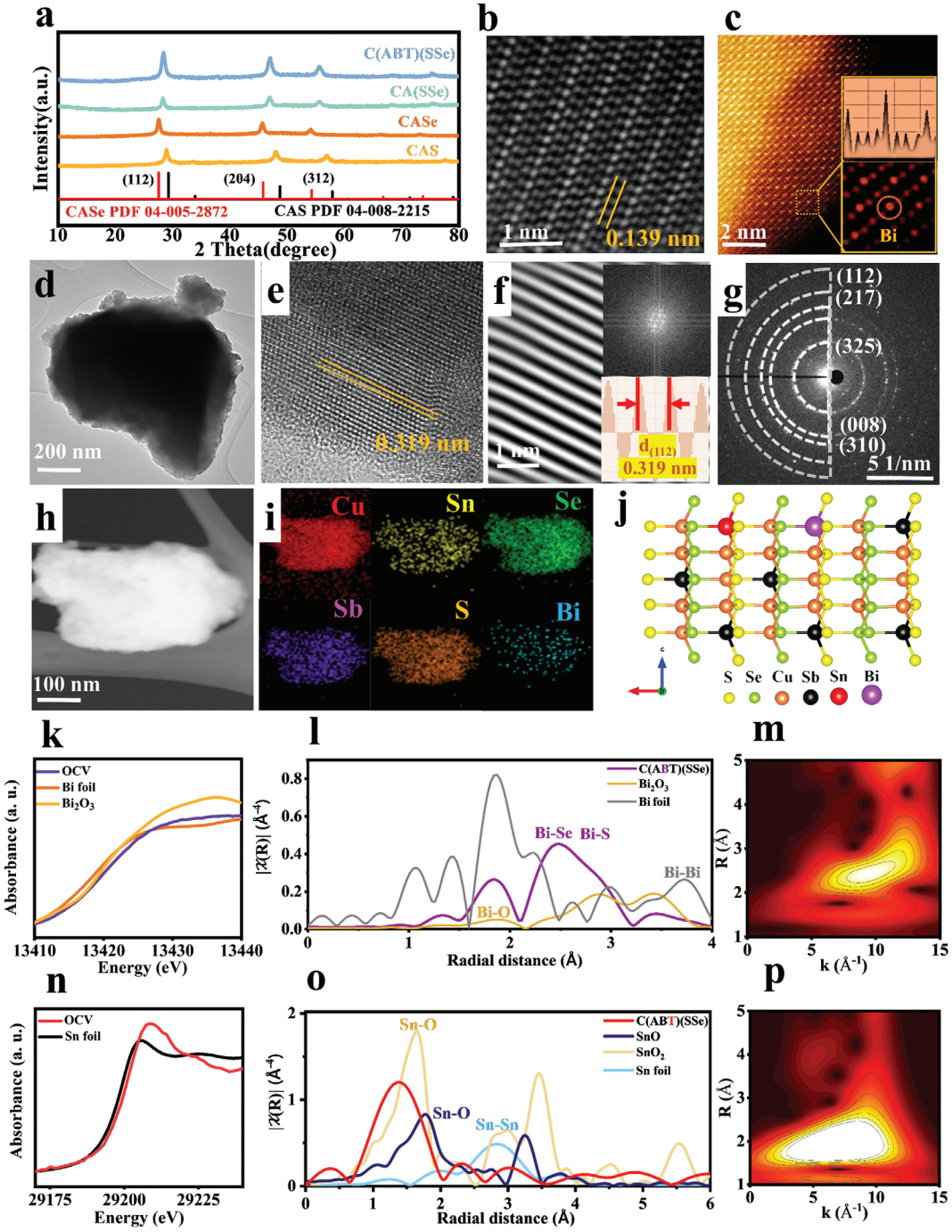

Figure 2. Morphology and structure characterization. a) XRD patterns, b) HRTEM image of C(ABT)(SSe). c) HAADF of Bi atom doped on the Sb site. d) TEM image. e) HRTEM image f) IFFT image. g) SAED pattern. h) HAADF image of C(ABT)(SSe). i) EDS elemental mapping of C(ABT)(SSe) j) Crystal structures of C(ABT)(SSe). k) Bi L III-edge XANES spectra, l) FTs of k^3-weighted Bi L III-edge EXAFS spectra of C(ABT)(SSe). m) Wavelet transforms for the Bi K-edge EXAFS signals for C(ABT)(SSe). n) Sn k-edge XANES spectra, o) FTs of k^3-weighted Sn k-edge EXAFS spectra of C(ABT)(SSe). p) Wavelet transforms for the Sn k-edge EXAFS signals for C(ABT)(SSe).

2.2. Morphology and Structure Characterization

C(ABT)(SSe) with entropy adjustment was prepared via high-energy ball milling, while CAS, CASe, and CA(SSe) crystallized in the tetragonal crystal system within the I4-2m space group, consistent with the host material. The X-ray diffraction (XRD) patterns of C(ABT)(SSe), CA(SSe), CAS, and CASe show that as Se content increases, there is a noticeable shift towards lower diffraction angles in all peaks (**Figure** 2a). Specifically, the lattice constants for CASe are a = 0.501 nm and c = 1.450 nm,

for CA(SSe) they are a = 5.421 nm and c = 1.170 nm, and for CAS, a = 5.302 nm and c = 1.080 nm. The larger ionic radius of Se (0.198 nm) compared to S (0.184 nm) causes linear changes in the lattice constants a and c with increasing Se content, confirming the successful solvation of Se atoms into the S sites according to Vegard's law (Figures S4 and S5, Supporting Information). Furthermore, XRD analysis of C(ABT)(SSe) and CA(SSe) reveals peak angles at 28.427° and 28.306°, 47.095° and 46.975°, and 55.610° and 55.493°, respectively, for the (112), (204), and (312) diffraction planes. These slight variations in peak angles are due to the presence of Bi and Sn in the entropy-adjusted C(ABT)(SSe) structure, with the minor deviations linked to the larger ionic radius of Bi (0.108 nm) compared to Sn (0.071 nm) and Sb (0.092 nm), causing a lower angular shift. For CAS and CASe, the diffraction angles are consistently noted at 28.910° for the (112), (204), and (312) planes.

The diffraction angles of CAS and CASe for the (112), (204), and (312) planes are 28.910° and 27.581°, 47.941° and 45.645°, 57.004° and 54.104° respectively (Figure 2a). The morphology and crystal structure of the entropy-regulated C(ABT)(SSe) were examined using a scanning electron microscope (SEM) and a spherical aberration-corrected scanning transmission electron microscope (Cs-corrected STEM) (Figure 2b). SEM images reveal that the crystals are similar in shape and size, indicating uniform stirring during the ball milling process (Figure S6, Supporting Information). Atomic doping creates defects in the material, increasing the number of active sites (Figure S7, Supporting Information). The STEM image of C(ABT)(SSe) shows an interatomic spacing of 0.139 nm on the (008) surface. Additionally, the intensity distribution in the HRTEM image highlights the Sb site doped with Bi, as indicated by the orange dotted box in Figure 2c. TEM images reveal the morphology of the material, with Figure 2d showing that C(ABT)(SSe) is composed of nanoparticles, synthesized via high-energy ball milling for improved reactivity in electrochemical reactions. HRTEM image captured the lattice arrangement, and inverse fast Fourier transform (IFFT) images confirmed a lattice distance of 0.319 nm from the (112) surface (Figure 2e–g). The regular arrangement at the Sb site incorporating Bi atoms demonstrates the successful use of entropy adjustment in CA(SSe). The atomic order of Sn closely resembles that of Sb, suggesting further analysis with X-ray absorption spectroscopy (XAS) to explore the chemical environment. These images were compared with surrounding radiation. High-angle annular dark field (HAADF) STEM images and energy dispersive spectroscopy (EDS) results, shown in Figure 2h–i, reveal uniform distribution of Cu, Sb, Bi, Sn, S, and Se in the nano-grains of C(ABT)(SSe), with no element agglomeration. To determine the composition of each atom in C(ABT)(SSe), inductively coupled plasma–optical emission spectroscopy (ICP-OES) was performed and the contents followed the expected settings (Table S1, Supporting Information). This demonstrates a successful synthesis of the entropy-adjusted material through multi-element doping. The structure of the material is depicted using the simulation software Vesta, demonstrating that C(ABT)(SSe), synthesized through non-stoichiometric entropy adjustment, is successfully constructed (Figure 2j). The X-ray photoelectron spectroscopy (XPS) analysis of C(ABT)(SSe) shows the Bi 4f spectra have two pairs of peaks corresponding to Bi-S and Bi-Se bonds.[5] The Sb 3d XPS spectra are located at 529.6 and 539.0 eV attributed to Sb^{5+}. Compared to other materials, the Sb 3d binding energy in C(ABT)(SSe) is lower than the CASSe (529.7 eV/ 539.1 eV) CAS(530.0 eV/ 540.2 eV) and CASe(530.5 eV/ 539.6 eV), which is attributed to its lower vacancy formation energy (Figures S8–S11, Supporting Information).[50]

To further analyze the structure and coordination environment, X-ray absorption near-edge structure (XANES) spectra at the Sb-K, Sn-K, and Bi-L III edges were measured. The Bi-L III edge spectra of C(ABT)(SSe), compared to Bi_2O_3 and Bi foil in Figure 2k, show that the energies are closer to Bi_2O_3, indicating that the chemical valence of Bi in C(ABT)(SSe) is similar to the Bi^{3+} in Bi_2O_3 (Figure 2k).[51] Since trace amounts of Bi and Sn are doped at the Sb site, distinguishing their changes via X-ray diffraction is challenging. To further analyze the chemical environment, uses Fourier transform (FT) on the EXAFS spectrum of the k^3-weighted Bi L III edge, mapping it as a function of the non-phase-corrected radial distance R. This is done alongside FT on the absorption spectra of Bi_2O_3 and Bi foil for comparison, helping to delineate the subtle chemical variations at the site. Artemis simulations performed to fit the R-space of Bi and Sn doped in Sb sites show curvilinear agreement, indicating that the doping of Bi and Sn in Sb sites within CAS and CASe structures achieves a good fit for these elements in the I4-2m space group (Figure S12, Supporting Information). The Bi peaks in the R-space of C(ABT)(SSe) do not overlap with Bi-Bi, confirming no Bi-Bi bonding occurs, and Bi is bonded to Se and S at 2.4 Å. The results align with findings from HRTEM and EDS (Figure 2l). To further interpret the Fourier transform outcomes, EXAFS wavelet transform (WT) analysis confirms the atomic configuration of Bi, with WT contours showing maximum intensity near 9.5 $Å^{-1}$ (Figure 2m). Additionally, the Sn K-edge XANES spectra of C(ABT)(SSe) and Sn foil show that the energies of C(ABT)(SSe) are higher than those of Sn foil, indicating non-zero valence states (Figure 2n). The R-space analysis from the Fourier transform of C(ABT)(SSe), SnO, SnO_2, and Sn foil reveals that the bond lengths of Sn in Sn foil, SnO, and SnO_2 differ from those of Sn doped at the Sb site, where Sn forms bonds with Se and S at 2.4 Å (Figure 2o).[52,53] The EXAFS wavelet transform (WT) shows maximum intensity near 9 $Å^{-1}$ (Figure 2p). Additionally, XANES analysis confirms the similarity in the chemical environments of Bi and Sn, demonstrating the effectiveness of non-stoichiometric strategies in creating new C(ABT)(SSe) materials for PIBs.

2.3. Electrochemical Performances of Configurational Entropy

Electrochemical testing was conducted within the voltage range of 0.01–3 V to explore the influence of dual-site doping with multiple potassium-ion active elements on configurational entropy for electrochemical performance. C(ABT)(SSe), CA(SSe), CAS, and CASe are mixed with N-doped graphene. The Raman spectrum reveals a relative intensity ratio of 0.84 for the D band (1350 cm^{-1}) to the G band (1580 cm^{-1}) (Figure S13, Supporting Information). TGA curves show that N-doped graphene content is 15.34% (Figure S14, Supporting Information). Half-cell performance of N-doped graphene exhibits 100 mAh g^{-1} capacity at 500 mA g^{-1}(Figure S15, Supporting Information). The SEM images of N-doped graphene are shown in (Figure S16,

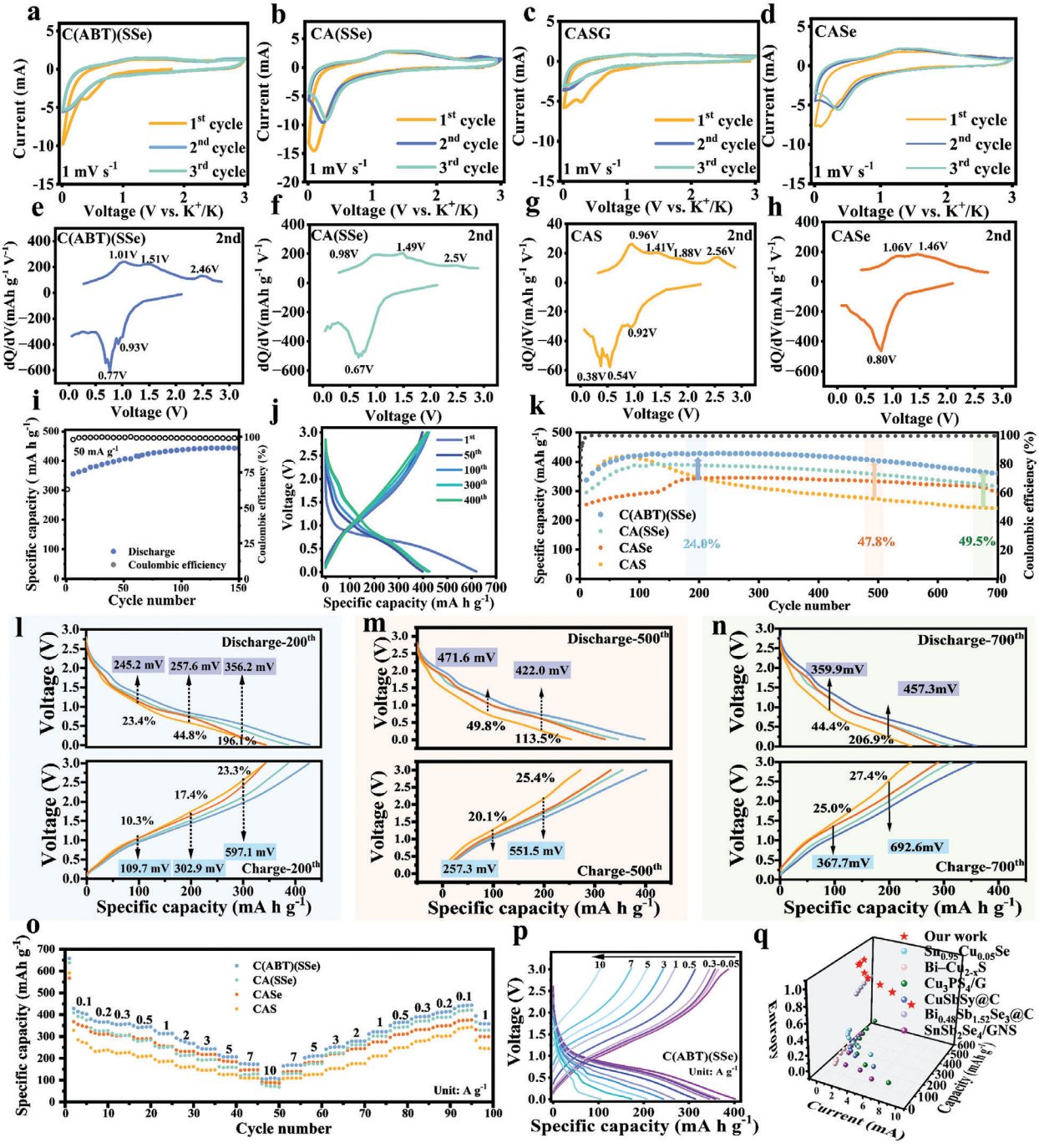

Figure 3. Electrochemical performance of the electrodes with different entropy values. a–d) First three-cycle CV profiles, and e,f) differential capacity plots of C(ABT)(SSe), CA(SSe), CAS and CASe. i) Cycling performance of the C(ABT)(SSe) electrodes at 0.05A g^{-1}. j) QV profile of C(ABT)(SSe) at different cycles. (k) Long-term cycling performance. l–n) GCD curves of C(ABT)(SSe), CA(SSe), CAS and CASe for 200th, 500th, 700th at current density of 500 mA g^{-1}. o) Rate performances. p) GCD curves of C(ABT)(SSe) at different currents. q) Rate performance comparison of C(ABT)(SSe) with previously reported anode materials.

Supporting Information). **Figure** 3a–d depicts the cyclic voltammetry (CV) curves of C(ABT)(SSe), CA(SSe), CAS, and CASe. Figure 3a shows notable overlap in the CV after the second cycle, indicating substantial overlap between the oxidation-reduction peaks and demonstrating good electrochemical reversibility, while CAS exhibits slight deviations. Figure 3e–h demonstrates the dQ/dV curves of the four materials during the second cycle, revealing two distinct reduction peaks observed at 0.77 and 0.93 V. The anodic peak at 1.01 V is associated with the dealloying of Sb, while the oxidation peaks at 1.51 and 2.46 V are

linked to the gradual depotassiation process. The dQ/dV curves exhibit distinctive features compared to unmodified materials, indicating that the multiple-element tuning strategies significantly influence the progress of oxidation and reduction reactions. C(ABT)(SSe) demonstrates a high capacity of up to 442.89 mAh g^{-1} at a current density of 50 mA g^{-1} (Figure 3i). Further analysis of the QV curves during 50, 100, 300, and 400 cycles at 500 mA g^{-1} reveals consistent reaction plateaus, underscoring the notable reversibility of C(ABT)(SSe) (Figure 3j). The synergistic effect of S and Se contributes to the host material's relatively superior conductivity and capacity. Moreover, the co-doping of bimetallic elements provides more stable active sites at the Sb site, resulting in excellent electrochemical performance. Due to the entropy regulation effect, C(ABT)(SSe) demonstrates a 24% higher capacity compared to undoped CAS at 200 cycles. As the number of cycles increases, the capacity become more pronounced, showing a 47.8% increase at 500 cycles and reaching 49.5% at 700 cycles. Remarkably, C(ABT)(SSe) retains a capacity retention of 84.3% after 700 cycles. In contrast, CAS retains only 42% after only 100 cycles due to the ineffective suppression of the shuttle effect (Figure 3k). Due to the electrode materials being mixed with N-doped graphene via high-energy ball milling before electrochemical long-cycle testing, initial charge-discharge cycling causes cracks on the surface of the sheets. These cracks increase the surface area contact between the internal materials and the electrolyte, resulting in a rise in capacity over the first 200 cycles. Unlike C(ABT)(SSe), CA(SSe), and CAS, CASe does not contain sulfur in its composition. Therefore, its trend of capacity increase differs. Previous reports have mentioned that although selenium-based compounds typically have lower capacity than sulfur-based compounds in potassium-ion batteries, they usually exhibit more stable cycling performance. Consequently, CASe shows a better capacity retention rate compared to CAS after 140 cycles.[16] Owing to the provision of effective active sites and multi-electron transfer at the Sb site, this efficiency advantage persists in the C(ABT)(SSe) even after 500 and 700 cycles. Additionally, for outstanding performance in practical applications, a high charge capacity below 1 V for potassium storage is also crucial. A higher charge capacity below 1 V for the anode indicates enhanced electrochemical activity and greater storage capacity for potassium ions at lower potentials. This suggests that the anode material has more active sites, such as defects, pores, and functional groups, which contribute to the improved performance and stability of the battery during charge-discharge cycles. Such characteristics are crucial for achieving efficient energy storage and fast charging capabilities in potassium-ion batteries. As shown in Figure 3l–n, thanks to the entropy adjustment strategy, C(ABT)(SSe) exhibits a higher charge capacity below 1 V across various cycle numbers.[54,55]

To elucidate the impact of configurational entropy differences between C(ABT)(SSe) and CAS, potential difference analysis was conducted at 200, 500, and 700 cycles (Figure 3l–n). At 200 cycles, charge/discharge overpotential gaps are 245.2/109.7 mV, and 257.6/302.9 mV for 100 and 200 mAh g^{-1}. As the number of cycles increases, the overpotential difference between the two becomes larger. At 700 cycles, the charge/discharge overpotential gaps are 359.9/367.7 mV and 457.3/692.6 mV for 100 and 200 mAh g^{-1}, respectively. These results show that the charge/discharge overpotential gap becomes larger at 200 mA h g^{-1} from 200 cycles to 700 cycles. Notably, C(ABT)(SSe) exhibits lower overpotential after 700 cycles because it can be optimized 206.9%/27.4% charge/discharge overpotential of CAS. Therefore, the entropy regulation effect is closely linked to the overpotential, resulting in higher capacity. Comparison of these overpotential differences indicates that materials with higher entropy demonstrate higher efficiency in chemical reactions when the charge-discharge cycles increase, especially exhibiting optimal performance after 200 cycles. With cycling, the highly reactive Sb sites benefit increasingly from the synergistic effects of cation doping, owing to their inherently higher conductivity and greater electron transfer. Additionally, the rate performance of the four materials was tested at current densities ranging from 0.1 $g^{-1}$to 10 A g^{-1}. C(ABT)(SSe) exhibited a capacity of 428.08 mAh g^{-1} at 0.1 A g^{-1}, gradually decreasing to 108.35 mAh g^{-1} at 10 A g^{-1} (Figure 3o,p). It's worth noting that C(ABT)(SSe) has an energy retention of 103% after returning to 0.1 A $g^{-1}$and has 70% higher capacity at 1 A g^{-1}, underscoring the influence of the entropy adjustment strategy on electrochemical performance. The synergistic effects of various potassium-reactive elements result in rapid potassium ion diffusion, further promoting enhanced capacity and durability under high-current testing. The QV curves at different currents remain smooth regardless of the rate. Notably, materials with both conversion-type and alloying-type reactions, like Bi(Cu_{2-x}Sn), which use a cationic source to regulate grain growth, display poorer multiplicity performance despite incorporating highly conductive Cu with Bi and Sn cations. $SnSb_2Se_4$ inherits the advantages of the binary Sb_2Se_3 and SnSe demonstrates improved electrochemical properties by integrating Sn into Sb_2Se_3, leveraging the synergistic effect of ternary compounds. Additionally, the $Bi_{0.48}Sb_{1.52}Se_3$@C formulation reduces volumetric expansion during redox reactions due to the synergistic effect between Bi and Sb alloying elements. The rate performances of these materials are notable: Bi(Cu_{2-x}Sn) reaches a capacitance of about 130 mAh g^{-1} at 0.8 A g^{-1}, while $Bi_{0.48}Sb_{1.52}Se_3$@C and $SnSb_2Se_4$/GNS achieve excellent rate performances at 1 and 6 A g^{-1}, respectively. Due to the doping of dual-element sites, C(ABT)(SSe) exhibits only a capacity decay rate of 45.9% from 0.1 to 2 A g^{-1}, whereas the similar $SnSb_2Se_4$/GNS suffers a severe 67.4% decay.[56–61] The effect of suppressing volume expansion is proved by SEM images. After cycling 100 times at 2000 mA g^{-1}, the expansion degree of the electrodes was measured for CAS and C(ABT)(SSe). It was found that CAS had a higher expansion rate of 62.83% after 100 cycles, while CABTSSe exhibited only a 7.63% increase in thickness. Due to the severe volume changes in CAS, its capacity rapidly declined after 100 cycles and the cycling performance was less than ideal. In contrast, CABTSSe maintained superior capacity retention. The surfaces of C(ABT)(SSe) and CASSe remained smooth and flat, similar to their pre-cycle states. However, noticeable cracks emerged on the CAS. Therefore, the entropy adjustment strategy successfully suppressed surface cracking (Figures S17 and S18, Supporting Information). These materials exhibit both conversion-type and alloy-type reactions, contributing to their high performance. Strengthening the synergistic effects during potassium ion charging and discharging could further improve multiplicity performance (Figure 3q). Compared to similar materials, our approach surpasses the original electrochemical performance limits of CAS, demonstrating that rational

adjustment of configuration entropy is an effective strategy. The synergistic effect of the multi-element regulation strategy modifies the local physical properties and chemical environment of the C(ABT)(SSe), thereby enhancing the electrochemical performance.

2.4. Synchrotron X-Ray Absorption Spectroscopy Study

To investigate the charge compensation mechanism of Bertholide in PIBs, we employed in situ X-ray absorption near-edge structure (XANES) and extended X-ray absorption fine structure (EXAFS) spectroscopy (**Figure 4a**). These techniques provided insights into the microstructures, chemical bonds, and electronic structures. Additionally, in situ K-edge X-ray absorption spectroscopy (XAS) was utilized to analyze the electrochemical behavior of Sb sites. The in situ k-edge absorption spectrum of Sb, depicted through contour-color fill, reveals an energy increase of 1.557 eV upon discharging to 0.01 V, leading to the reversible formation of K_3SbS_4 and K_3SbSe_4—effective conductors for PIBs—with the Sb oxidation state consistently at 5^+, indicating significant charge transfer and enhanced electrochemical performance (Figure 4b).[62] When charging, the Sb signal shifts to a higher energy position by 5.985 eV. Plotting the energy change and potential against the charging and discharging power clarifies the impact of energy shifts on valence changes and battery performance. During discharge, the conversion reaction starts at 0.97 V, with an energy increase observed at 0.43 V. This suggests that partial detachment of Sn increases Sb's energy, while Sn levels decrease upon further discharging. During charging, an increase in energy between 1.01 and 1.51 V was observed as Sb in K_3(Sb, Bi) reversibly reverted to the raw material through depotassiation (Figure 4c,d). The in situ XANES, displayed on a 3D colorman surface, showed a slight energy increase in the Sb K-edge absorption spectra due to the redox reaction, while the Fourier-transformed EXAFS spectra revealed changes in bond lengths and a reduction in peak sizes, indicating a decreased coordination number around the Sb K-edge, which facilitates the acceptance of other atoms or molecules and accelerates the electrochemical reaction. The initial K-edge curve energy of Sb, higher than that of Sb foil and Sb_2O_3, indicates an Sb^{5+} valence state consistent with Sb in entropy-adjusted C(ABT)(SSe) (Figure 4e–h). The rising energy trend after discharging and during charging suggests that multi-element doping modifies the redox products of Sb with potassium ions and slightly elevates the Sb valence, enhancing charge transfer and accounting for the increased capacitance observed in the first 100 cycles compared to CAS.[62,63] C(ABT)(SSe) maintains superior capacity in later cycles, with the Sb valence consistently around 5^+ and minimal bond length changes, indicating a stable chemical environment conducive to forming K_3SbS_4 and K_3SbSe_4 (Figure 4i–n). This stability suggests sustained charge transfer over numerous electrochemical cycles, evidenced by stable CV cycle performance. Furthermore, the Bi-L III edge experiences an energy decrease of −1.818 eV when discharged to 0.01 V due to the alloying reaction with Sb forming K_3(Sb, Bi), and an energy increase of +1.205 eV upon recharging to 3 V, nearly returning to the initial position. The energy nearly returns to its initial state but isn't entirely reversible, as evidenced by the constant EXAFS peak positions at OCV and 3 V, though the peak slightly diminishes. The energy change in the Sn element at the K-edge is −2.819 upon discharge and +2.819 on recharge, with a minor increase in EXAFS observed over time post-cycling (Figure 4o). The chemical environments of Bi and Sn are consistent between the initial state and after one cycle, indicating their valence states are similar and reversible at the Sb site. This suggests that the synergistic effect of precise non-stoichiometric modulation among the three alloying elements remains critical for electrochemical reactions and essential for activating Sb in subsequent stages.

The XANES spectra of Sb, Bi, and Sn samples reveal significant energy shifts and valence changes, indicating strong interactions with K^+. The regulation of metallic element doping impacts not only the initial physical and chemical properties of the material through structural design but also plays a consistent role during the charging and discharging processes, influencing subsequent chemical reactions. Wavelet transforms (WT) and a 3D color map surface were employed to analyze structural changes in the Sb site during the charge/discharge process. A decrease in intensity and a slight shift to a lower radial distance in the Sb signal indicate increased structural disorder, suggesting enhanced entropy modulation. This disorder correlates with improved chemical reactivity, higher configuration entropy, and better rate performance in electrochemical capacity. The Sb peak at around 2 Å, representing bond lengths with S and Se, indicates strong bonding in the pristine state. Initially, the dopant metals Bi and Sn share similar chemical environments with Sb (**Figure 5a–c**). However, after discharge, they exhibit distinct radial lengths: Sn shows a radial length of 1.5 Å at 0.01 V, suggesting bonding with K, though this is less visible due to Sn's minimal concentration (Figure 5g–i). On returning to 3 V, Sn's radial length and valence revert to those of the initial state, indicating Sn's return to the original Sb site and the formation of non-stoichiometric compounds post-cycle. Bi and Sb are known to form a K_3(Bi, Sb) alloy-type reaction (Figure 5d–f), and this study confirms that even a small amount of Bi doping results in the formation of K_3(Bi, Sb). After recharging to 3 V, the radial length of 2 Å and the similarity to the peak potential of 9 $Å^{-1}$ in the wavelet transform (WT) indicate significant structural entropy reorganization following oxidative reduction. The increase in valence observed experimentally is key for improving electrochemical performance.

Ex-situ XPS analysis after 200 cycles compared the non-stoichiometric adjusted Sb alloy with other materials of lower configuration entropy. CAS and CASe, which have not undergone doping, showed energy shifts of −1.15 and −0.7 eV, respectively. CASe, in particular, displayed better cyclic properties than CAS, which shifted to more negative energy values (Figure 5j,k). In CA(SSe), the energy change is negligible, indicating that Se and S have no impact on the energy response of Sb elements post-reaction. However, in C(ABT)(SSe), the energy shift at 3 V shows a significant increase from the initial state, with a difference of 1.2 eV, indicating that activated Sb sites facilitate enhanced charge transfer over multiple charge-discharge cycles. This is a result of incorporating additional elements Bi and Sn. **Figure 6l–o** shows the HRTEM and SAED of C(ABT)(SSe) at 0.01 and 3 V during the first cycle. When discharged to 0.5 V, K_3SbS_4 and K_3SbSe_4 are formed. Upon further discharge to 0.01 V, peaks of K_3(Bi,Sb) K_2Se and KS_2 appear. Upon recharge to 3 V, the

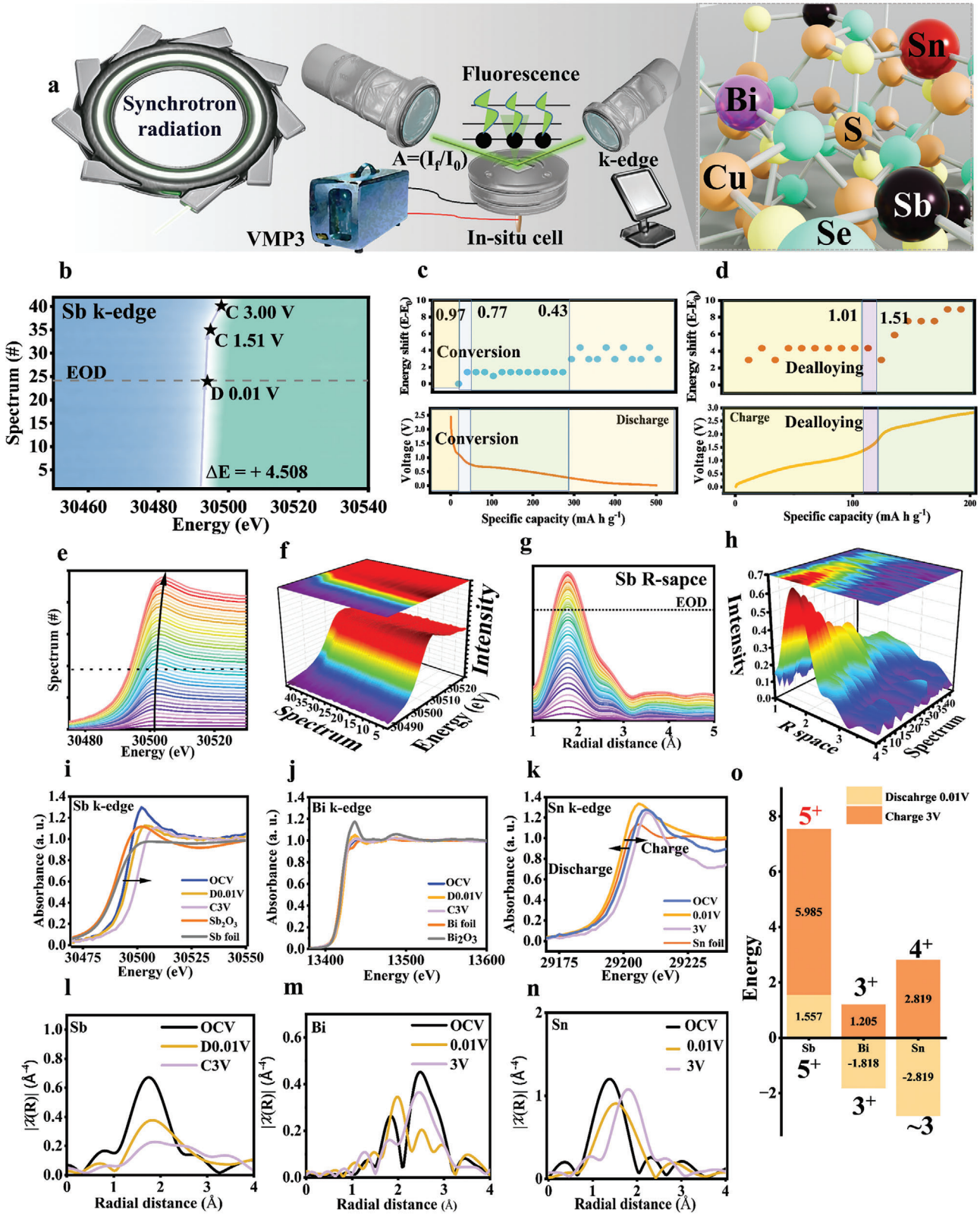

Figure 4. XAS of C(ABT)(SSe) electrode. a) Operando XAS experiment setting. b) Sb K-edge operando XANES spectra . c,d) Sb x-ray adsorbed energy change with QV. e,f) 3D color map surface of Operando Sb K-edge. g,h) 3D color map surface of Sb XANES. i–k) XAS of Sb, Bi, and Sn. l–n) EXAFS spectra of Sb, Bi, and Sn. o) Energy change of Sb, Bi, and Sn at first cycle.

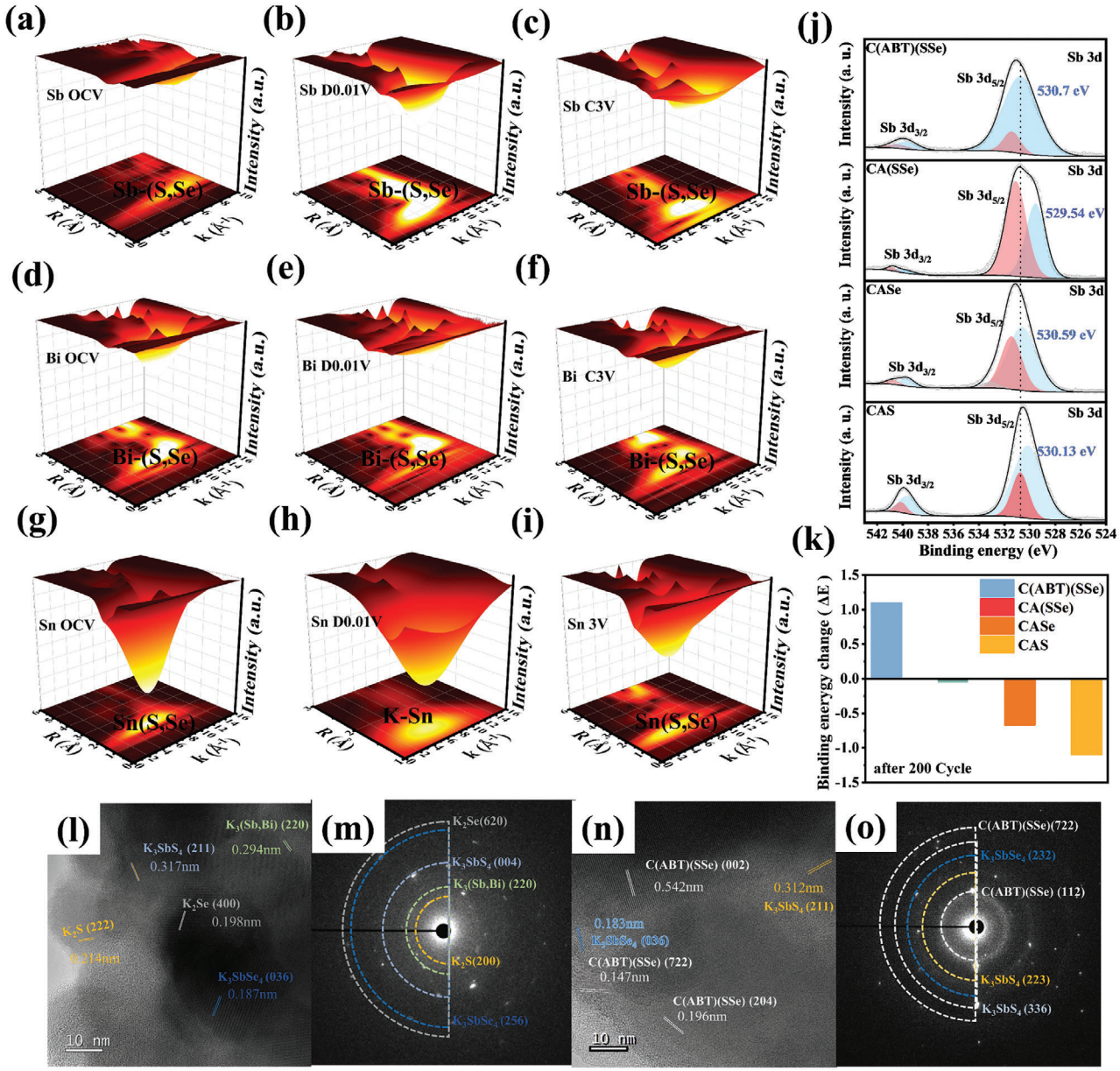

Figure 5. Operando and ex-situ analysis of K-ions storage mechanism of C(ABT)(SSe). a) OCV. b) Discharged to 0.01 V. c) Charged to 3 V of XANES of Sb. d) OCV. e) Discharged to 0.01 V. f) Charged to 3 V of ex situ XANES analysis of Bi. g) OCV. h) Discharged to 0.01 V. i) Charged to 3 V of ex situ XANES of Sb. j) Ex situ XPS of Sb at C3C after 200 cycles. k) Binding energy change of Sb after 200. (l-o) HRTEM and SAED analysis of C(ABT)(SSe) at 0.01 and 3.0 V, respectively.

peak of C(ABT)(SSe) reappears (Figure S19, Supporting Information). Due to the presence of these tiny cells, it is challenging to observe the structural changes of C(ABT)(SSe) during charge/discharge in in situ XRD tests (Figure S20, Supporting Information). The lattice spacings of 0.317, 0.294, 0.214, 0.198, and 0.187 nm at 0.01 V represent the (022), (220), (222), (400), and (036) crystal planes of K_3SbS_4, $K_3(Bi,Sb)$, K_2S, K_2Se, and K_3SbSe_4, respectively. Notably, K_3SbS_4 is a promising sulfide-based K-ion conductor.[64] After charging to 3 V, The lattice spacings of 0.183, 0.312, 0.196, 0.542, and 0.147 nm represent the (036), (211), (204), (002), and (722) crystal planes of K_3SbSe_4, K_3SbS_4, and the remaining three crystal planes represent C(ABT)(SSe). Evidence of Sb bonding with S and Se during the reaction is demonstrated again in Figure 6l. Lastly, the EDS mapping shows the compound at 0.1 and 3 V without apparent phase separation (Figures S21 and S22, Supporting Information).

2.5. The Potassium Ion Kinetics Analysis

To explore the impact of configuration entropy on electrochemical properties, advanced characterization techniques such

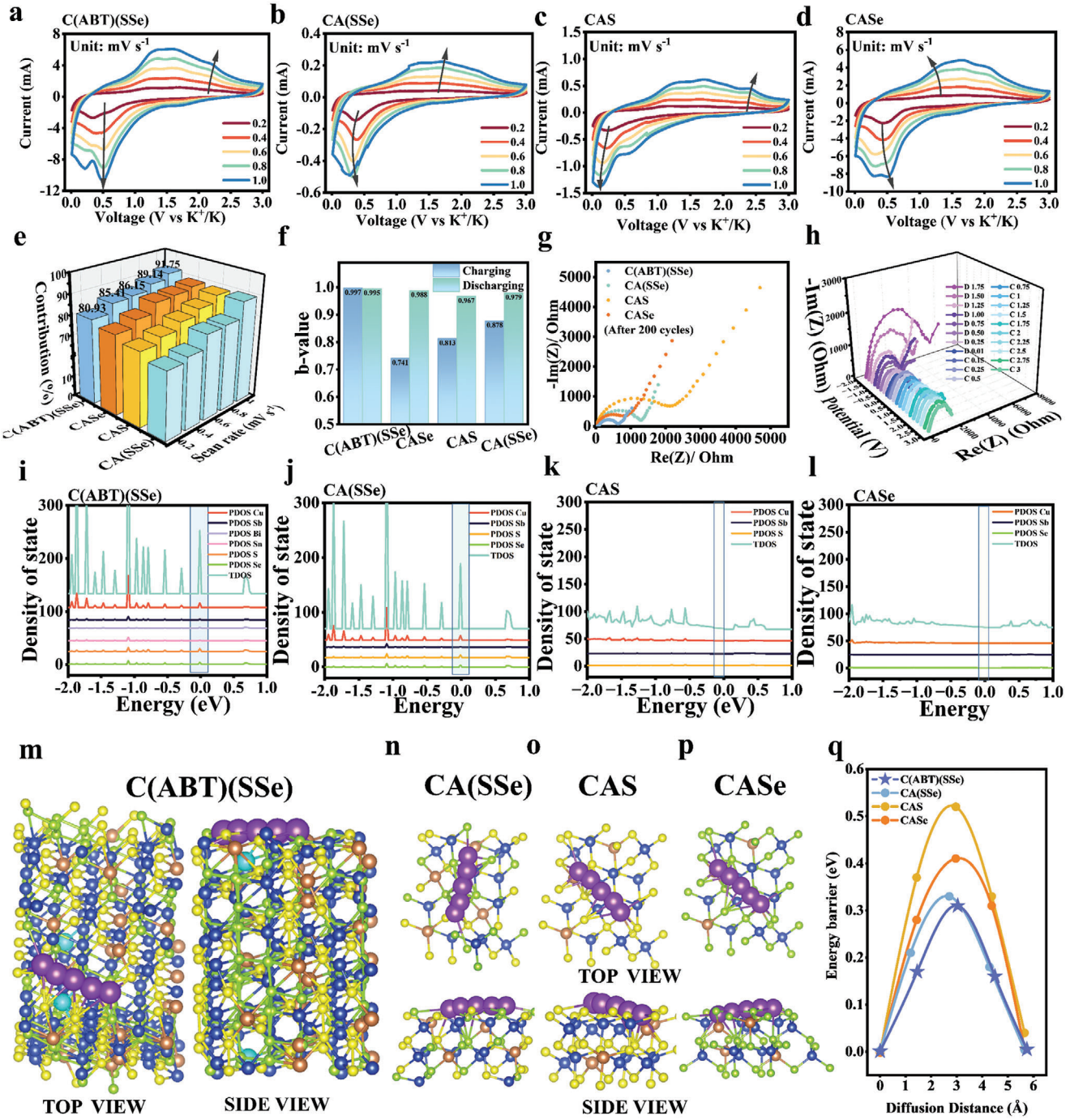

Figure 6. Electrochemical kinetic behaviors and simulations of C(ABT)(SSe). a–d) CV curves at various scan rates in the range of 0.2–1.0 mV s^{-1}. e) Comparison of contribution ratio at different scan rates. f) b value. g) EIS at 200 cycles. h) In situ EIS of C(ABT)(SSe) at first cycle. i–l) PDOS simulation. m–p) NEB simulation of diffusion energy barriers. q) Comparison of K-ion diffusion energy barriers for C(ABT)(SSe), CA(SSe), CAS, and CASe.

as cyclic voltammetry (CV), Electrochemical Impedance Spectroscopy (EIS), and the climbing image nudged elastic band (CI-NEB) method were utilized. The kinetics of K^+ storage were examined in four materials—C(ABT)(SSe), CA(SSe), CAS, and CASe—through CV measurements at various scan rates (Figure 6a–d). The CV curves were analyzed to assess the capacitive contributions of the materials, with the total current response (i) at a fixed potential (V) being described by the following equation: $i = (k1\nu) + (k2\nu^{\frac{1}{2}})$, where $k1\nu$ and $k2\nu^{\frac{1}{2}}$ represent the contributions from capacitance-controlled and diffusion-controlled processes, respectively.[65] The capacitance values of C(ABT)(SSe), calculated based on this equation, were found to

be 80.95%, 85.41%, 86.15%, 89.14%, and 91.75%, corresponding to scanning rates of 0.2, 0.4, 0.6, 0.8, and 1.0 mV s^{-1}, respectively (Figure 6e; Figure S23a,c,d, Supporting Information). From the GITT measurement, it can be observed that C(ABT)(SSe) exhibits an initial discharge diffusion coefficient of 9.66×10^{-11} cm^2 s^{-1}, while CAS shows a significantly lower value of 3.15×10^{-11} cm^2 s^{-1}. Thanks to the cations and anions co-doping properties, the initial diffusion coefficient of C(ABT)(SSe) is three times higher than that of CAS and consistently maintains the superior diffusion coefficient during subsequent discharge and charge cycles(Figure S24, Supporting Information). By controlling the synergistic interactions of S, Se, Sb, Bi, and Sn, it promotes the thermal stability of vacancies, exposes more reactive sites, and boosts charge reactions, thereby improving the capacitive performance of Berthollide in PIBs. Consequently, this non-stoichiometric design optimization of the active surface contributes to faster electrochemical K^+ storage, leading to enhanced rate capability. Thus, C(ABT)(SSe) displays superior performance in rate performance tests and exhibits a higher charge-discharge capacity even at high currents of up to 10A g^{-1}. To further understand the entropy adjustment process and discern the existence of redox involving the transfer of electrons, the relationship between the current density (I) and sweep speed (V) can be expressed by the equation $ip = av^b$, where the Tafel slope is obtained by taking the logarithm of the equation. The Tafel slope, denoted by *b*, indicates the nature of the capacitance control process, with typical values ranging from 0.5 to 1. 0.5 suggests a diffusion-controlled process, while 1.0 points to surface capacitance control. Analyzing *b* offers insights into the entropy adjustment process and the roles of oxidation and reduction reactions. Differences in reaction kinetics between C(ABT)(SSe) and the others become clear by observing their electron transfer redox reactions. These *b*-values, reflecting the current-potential relationship during charging and discharging, are crucial for understanding reaction rates. The b values of the anode and cathode current peaks of CAS, CA(SSe), CASe, and C(ABT)(SSe) were 0.995, 0.979, 0.979, and 0.967 (anodic), and 0.997, 0.878, 0.741, and 0.813, respectively (cathodic) (Figure 6f; Figure S23b, Supporting Information). These higher *b*-values suggest a greater sensitivity of the electrode reaction rate to potential changes, illustrating that the C(ABT)(SSe) was mainly under surface control. Additionally, by doping Bi and Sn with non-stoichiometric engineering and configuration entropy enhancement, the synergistic effects modify the chemical environment at the Sb site, activating the alloying/dealloying process in C(ABT)(SSe). The Tafel slope close to 1, demonstrates the successful impact of higher K^+ chemical kinetics and electron transfer. Furthermore, electrochemical impedance spectroscopy (EIS) of C(ABT)(SSe) after 200 cycles showed reduced impedance, highlighting Sb's beneficial effect on conductivity following valence enhancement (Figure 6g). In situ EIS analysis during initial cycles showed a decrease in impedance to 2000 ohms in both charging and discharging, indicating enhanced charge release from active sites and subsequent reduction in impedance. The PDOS of C(ABT)(SSe), CA(SSe), CAS, and CASe are shown in Figure 6h. Compared to CAS, C(ABT)(SSe) exhibits six times the TDOS electronic states located at the Fermi energy level, indicating that the multi-element dopants are well-integrated and share comparable environments.

The climbing image nudged elastic band (CI-NEB) method is utilized in first-principles calculations to determine the energy barriers for ion migration along specific diffusion pathways in ionic conductors (Figure 6i–l). We hypothesize initial and final positions for potassium ion diffusion in the C(ABT)(SSe) (112) plane and suggest a possible migration path (Figure 6m–p). The structure likely supports multiple ion migration pathways by integrating additional K^+ and identifying a high-energy intermediate diffusion site, leading to varied energy barriers and anisotropic diffusion. The K^+ diffusion energy of C(ABT)(SSe) (0.31 eV) was lower than that of CA(SSe) (0.33 eV), while CAS exhibited the highest diffusion energy (0.52 eV) (Figure 6q), indicating that the K^+ diffusion energy is reduced by 40%. The synergistic effects of Sb, Bi, and Sn expose more chemical reaction sites.

2.6. Application in K-Ion Full-Cell and Pouch-Type Cell

At the core of the configurational entropy strategy is the precise manipulation of dopant atom placement, activation of dopant sites, and induction of defects. These processes collectively alter the diffusion energy and reactivity within the material system. Our subsequent studies demonstrate the practical application of PIBs. The PB half-cell delivered a capacity of 55.62 mA h g^{-1}at 250 mA $g^{-1}$and the CV curves of PB at different cycles are highly overlapping, indicating excellent cycling performance and stable capacity retention at 100 mA g^{-1}. After rate performance tests at 50, 100, and 150 mA g^{-1}, PB still retains a capacity close to its initial value when returned to 50 mA g^{-1}. More importantly, due to the high oxidation potential of polysulfide K_2S, certain cathode materials such as PTCDA and $KVPO_4F$ cannot achieve the required high working voltage of over 3.5 V.[66] Therefore, Prussian blue analogs with high working voltage are utilized. Given its superior electrochemical performance and characteristics, PB was chosen as the cathode for potassium-ion full batteries (Figures S25 and S26, Supporting Information). **Figure 7**a illustrates the structure of the potassium ion full cell. Figure 7b shows CV curve scanning of the full cell across three cycles, displaying consistent redox peaks that indicate good electrochemical reversibility. Figure 7c presents the QV plots for the C(ABT)(SSe)||PB full cell and its half-cell counterpart. The superior conductivity, higher configuration entropy, thermodynamically stable active sites, increased electron transfer, and rapid potassium ion diffusion enable C(ABT)(SSe) to maintain its optimal performance in practical applications for full cells. Therefore, the full cells maintain robust cycling performance at 300 mA g^{-1}, retaining 90.5% of its capacity after 400 cycles, demonstrating high reversibility and stability (Figure 7d). Compared to CAS||PB, the charging overpotential of C(ABT)(SSe)||PB is 258.9 mV at 200 mA g^{-1} with 17.8% initial capacity difference, indicating excellent initial cycle performance (Figure 7e). The superior performance in high-rate tests benefits from the high conductivity and improved properties brought by the configurational entropy effect. The capacity values at are 270.39, 262.59, 248.6, 220.03, 210.61, 202.78, and 195.0 mA g^{-1} at currents of 0.2, 0.3, 0.5, 1, 1.5, 2, and 3 A g^{-1} respectively (Figure 7f). When recharging at 0.2 A g^{-1}, the capacity recovery rate of C(ABT)(SSe)||PB is 99.6%. Moreover, Figure 7g shows QV curves with a minor over-potential

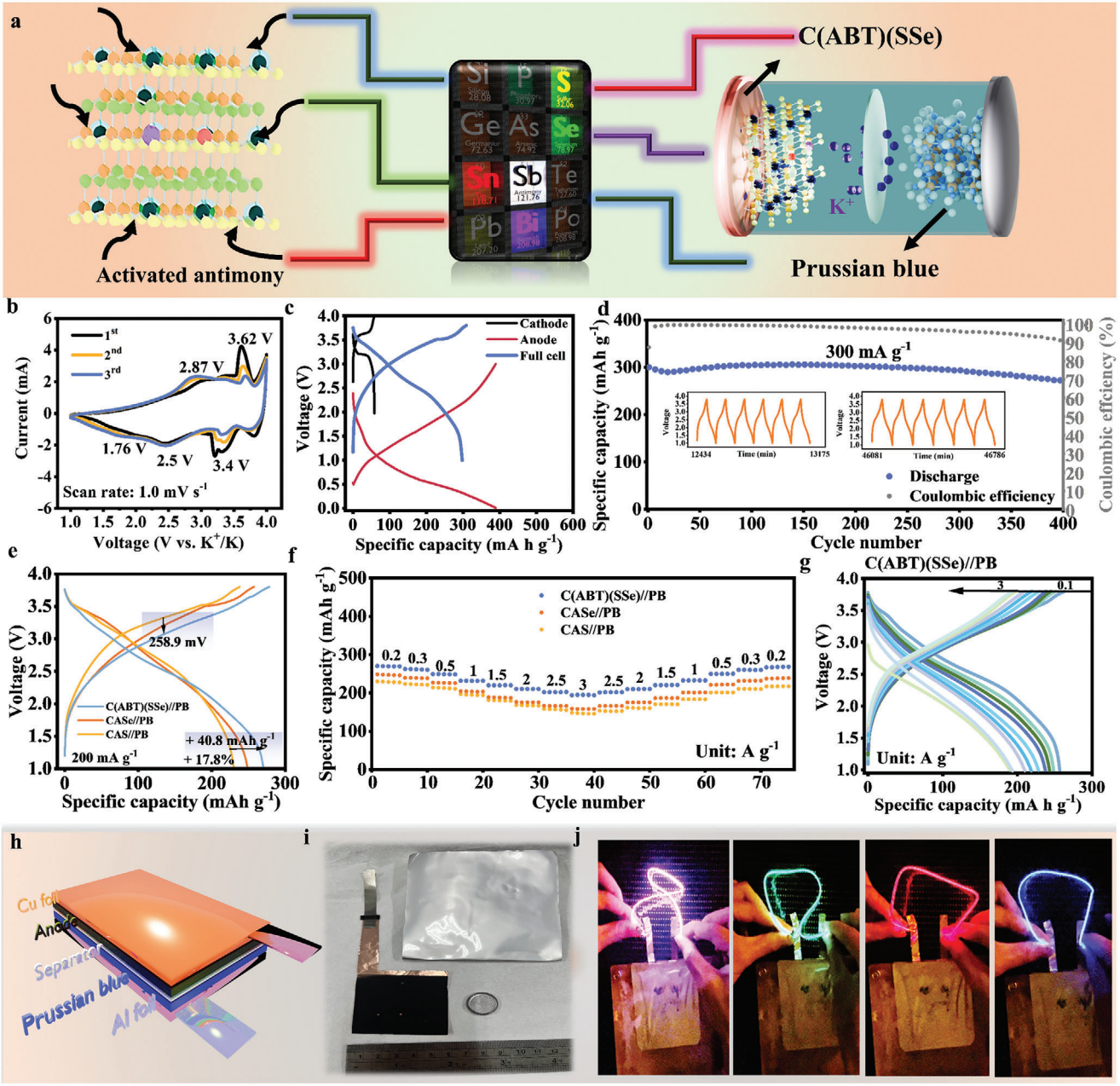

Figure 7. Electrochemical performances and practical application of C(ABT)(SSe)||PB. a) Scheme of PIBs full cells. b) CV curves of full cells at a scan rate of 1.0 mV s^{-1}. c) GCD curves of cathode, anode, and a full cells. d) Long-term cycling performance based on active material of anode at 300 mA g^{-1}. The inset shows the voltage profiles at specific cycles. e) GCD curves of different entropy materials. f) Rate performances of full cells. g) GCD curves of C(ABT)(SSe)||PB at different currents. h) Scheme of a pouch-type full cells. i) The size comparison of pouch-type battery to coin cell. j) Practical application of pouch-type full cells on different color LED light lines.

shift when increasing the current from 0.1 to 3 A g^{-1}, yet the similarity of the charging/discharging curves highlights excellent reversibility and robust rate performance in full cells. Consequently, C(ABT)(SSe)||PB shows 33.6% higher capacity at 3A g^{-1} and 7% less decay compared to CAS||PB full cells, demonstrating the extended electrochemical performance in full cells due to the precisely adjusted entropy and the synergistic multi-effect. Figure 7h presents a schematic of the potassium-ion pouch-type full cells and we extend the electrochemical testing from coin cells to pouch-type batteries to compare performance across different battery formats. The GCD curves and cycling stability are shown in (Figure S27, Supporting Information), demonstrating its considerable application prospects in energy storage devices. The anode was applied over a large 20cm^2 area and paired with the electrode to construct a pouch cell (Figure 7i,j). An LED light bar, requiring at least 3 V to operate, was used to demonstrate the potential application of this battery. The full cells reversible discharge at 3.4 V effectively powers the LED strip, consistently

illuminating pink, green, red, and blue LEDs, showing the material's suitability for diverse practical applications in pouch-type full cells.

3. Conclusion

In conclusion, we have successfully synthesized a non-stoichiometric compound, C(ABT)(SSe), featuring cation and anion co-doping to enhance PIBs anodes through an innovative entropy adjustment strategy. The incorporation of dopant significantly improved conductivity, while the dual-site conversion and alloying elements optimized ion diffusion, charge transfer, and electrode kinetics. By regulating configurational entropy, we created more active sites for Sb with thermodynamically stable defect active sites. Operando XAS analysis revealed that Sb ions in C(ABT)(SSe) maintained a high-valence state (Sb^{5+}) throughout multiple charge-discharge cycles. This was further corroborated by Ex situ XPS, which showed the persistence and increasing trend of high-valence characteristics over several cycles. Kinetic analysis demonstrated enhanced cycle stability and reduced resistance post-cycling due to entropy regulation. DFT calculations indicated a fourfold increase in DOS at the Fermi level for C(ABT)(SSe) compared to unregulated materials, enhancing electron presence and charge accumulation at high-configurational entropy Sb sites, resulting in higher defect thermodynamic stability and superior conductivity. The entropy regulation strategy unlocked high-valence alloy-type reactions, increasing capacity and rate performance. Bi and Sn cations at Sb sites effectively lowered the potassium ion surface diffusion energy barrier, improving potassium ion kinetics and electronic conductivity. The synergistic reaction of Sb, Bi, and Sn yielded high-valence Sb^{5+}, which provided superior rate performance and cycle stability. Additionally, the co-existence of S and Se preserved high capacity and stability, mitigating the original shuttle effect. This novel entropy regulation strategy demonstrated through precise doping and dual-site replacement, significantly enhanced the electrochemical performance of PIBs anodes by increasing thermodynamically stable active sites and lowering energy barriers. Our findings offer new insights into the design of multi-element configurational entropy materials, emphasizing their critical role in achieving superior electrochemical performance and stability in future battery anode materials.

Supporting Information

Supporting Information is available from the Wiley Online Library or from the author.

Acknowledgements

This work was supported by the financial support from the 2030 Cross-Generation Young Scholars Program by the National Science and Technology Council, Taiwan (NSTC 112-2628-E-007-010 and NSTC 112-2628-E-007- 016). The authors thank the technical support from Mr. Yung-Sheng Chen in the Instrumentation Center at National Tsing Hua University.

Conflict of Interest

The authors declare no conflict of interest.

Author Contributions

K.-S.J. and H.-Y.T. came up with the original idea and designed the experiments. Ying-Rui Lu helped the XAS experiments. M.-Y.L. and K.-Y.H. helped the HAADF-STEM experiments. K.-S.J., Y.-C.Y, and H.-Y.T. wrote the paper. The study was conceived and supervised by H.-Y.T.

Data Availability Statement

The data that support the findings of this study are available from the corresponding author upon reasonable request.

Keywords

berthollide, configuration entropy, full cell, potassium-ion batteries

Received: June 24, 2024
Revised: July 27, 2024
Published online:

[1] Y.-Y. Hsieh, H.-Y. Tuan, *Small* **2023**, *19*, 2370434.
[2] Y. X. Yao, X. Chen, C. Yan, X. Q. Zhang, W. L. Cai, J. Q. Huang, Q. Zhang, *Angew. Chem. Int. Ed. Engl.* **2021**, *60*, 4090.
[3] Y. Son, H. Cha, T. Lee, Y. Kim, A. Boies, J. Cho, M. De Volder, *Energy Environ. Mater.* **2024**, *7*, 12615.
[4] K. Zhang, Z. Hu, X. Liu, Z. Tao, J. Chen, *Adv. Mater.* **2015**, *27*, 3305.
[5] Y.-Y. Hsieh, H.-Y. Tuan, *Energy Storage Mater.* **2022**, *51*, 789.
[6] W. Feng, C. Pan, H. Wang, B. Zhang, W. Luo, C. Shen, J. Wang, C. Cheng, X. Xv, R. Yu, Y. Guo, L. Mai, *Energy Storage Mater.* **2023**, *63*, 102975.
[7] X. Wang, Z. Xiao, K. Han, X. Zhang, Z. a. Liu, C. Yang, J. Meng, M. Li, M. Huang, X. Wei, L. Mai, *Adv. Energy Mater.* **2023**, *13*, 2202861.
[8] X. Zhang, H. Zhu, Q. He, T. Xiong, X. Wang, Z. Xiao, H. Wang, Y. Zhao, L. Xu, L. Mai, *Adv. Funct. Mater.* **2022**, *32*, 2205330.
[9] Z. Xiao, F. Xia, L. Xu, X. Wang, J. Meng, H. Wang, X. Zhang, L. Geng, J. Wu, L. Mai, *Adv. Funct. Mater.* **2022**, *32*, 2108244.
[10] L. Wu, H. Fu, W. Lyu, L. Cha, A. M. Rao, K. Guo, J. Zhou, S. Wen, B. Lu, *ACS Nano* **2024**, *18*, 13415.
[11] M. Huang, B. xi, L. Mi, Z. Zhang, W. Chen, J. Feng, S. Xiong, *Small* **2022**, *18*, 2107819.
[12] Y. Cheng, Z. P. Yao, Q. B. Zhang, J. M. Chen, W. B. Ye, S. Y. Zhou, H. D. Liu, M. S. Wang, *Adv. Funct. Mater.* **2020**, *30*, 2005417.
[13] H. B. Ding, J. Wang, L. Fan, Z. M. Liu, X. X. Jia, X. Z. Yu, B. A. Lu, *Chem. Eng. J.* **2020**, *395*, 125147.
[14] M. Ma, S. Chong, K. Yao, H. K. Liu, S. X. Dou, W. Huang, *Matter* **2023**, *6*, 3220.
[15] B. B. Sheng, L. F. Wang, H. J. Huang, H. Yang, R. Xu, X. J. Wu, Y. Yu, *Small* **2020**, *16*, 2005272.
[16] W.-W. Shen, Y.-Y. Hsieh, Y.-C. Yang, K.-Y. Hsiao, M.-Y. Lu, C. W. Chou, H.-Y. Tuan, *Adv. Sci.* **2024**, *11*, 2308582.
[17] S. J. Wang, P. Xiong, X. Guo, J. Q. Zhang, X. C. Gao, F. Zhang, X. Tang, P. H. L. Notten, G. X. Wang, *Adv. Funct. Mater.* **2020**, *30*, 2001588.
[18] Y. Yang, J. Wang, S. Liu, W. Zhu, G. Ye, X. Yi, B. Lu, *Chem. Eng. J.* **2022**, *435*, 134746.
[19] D. Zhang, H. Hu, X. Ma, X. Yu, F. Li, J. Zhou, B. Lu, *Angew. Chem. Int. Ed. Engl.* **2024**, *63*, 202405153.
[20] Y. Yun, B. xi, Y. Gu, F. Tian, W. Chen, J. Feng, Y. Qian, S. Xiong, *J. Energy Chem.* **2022**, *66*, 339.
[21] Y. Yun, B. xi, F. Tian, W. Chen, W. Sun, H. Pan, J. Feng, Y. Qian, S. Xiong, *Adv. Energy Mater.* **2021**, *12*, 2103341.
[22] H. Jiang, X. Lin, C. Wei, J. Feng, T. Xuelei, *Small* **2021**, *18*, 2104264.

[23] H.-Y. Tuan, A. Ghezelbash, B. A. Korgel, *Chem. Mater.* **2008**, *20*, 2306.
[24] Q. Z. Wu, B. C. Chen, H. N. Xie, X. R. Bai, M. Liang, Z. Y. Wu, X. Y. Jin, C. N. He, N. Q. Zhao, *Chem. Eng. J.* **2022**, *430*, 132906.
[25] P. X. Xiong, J. X. Wu, M. F. Zhou, Y. H. Xu, *ACS Nano* **2020**, *14*, 1018.
[26] L. Feng, Z. Zhu, R. Yan, X. Fu, X. He, D. Wu, H. Li, Z. Guo, W. Yang, Y. Wang, *Adv. Sci.* **2023**, *10*, 2207584.
[27] W. Zhang, R. Huang, X. Yan, C. Tian, Y. Xiao, Z. Lin, L. Dai, Z. Guo, L. Chai, *Angew. Chem., Int. Ed.* **2023**, *62*, 202308891.
[28] X. Ge, S. Liu, M. Qiao, Y. Du, Y. Li, J. Bao, X. Zhou, *Angew. Chem., Int. Ed.* **2019**, *58*, 14578.
[29] Y. Du, W. Weng, Z. Zhang, Y. He, J. Xu, J. Sun, J. Liao, J. Bao, X. Zhou, *ACS Mater* **2021**, *3*, 356.
[30] J. Li, Y. Ren, Z. Li, Y. Huang, *ACS Nano* **2023**, *17*, 18507.
[31] G. Ding, M. Yao, J. Li, T. Yang, Y. Zhang, K. Liu, X. Huang, Z. Wu, J. Chen, Z. Wu, J. Du, C. Rong, Q. Liu, W. Zhang, F. Cheng, *Adv. Energy Mater.* **2023**, *13*, 2300407.
[32] T. He, S. Weng, Y. Ye, J. Cheng, X. Wang, X. Wang, B. Wang, *Energy Storage Mater.* **2021**, *38*, 389.
[33] D. Du, R. Zheng, M. He, C. Zhao, B. Zhou, R. Li, H. Xu, X. Wen, T. Zeng, C. Shu, *Energy Storage Mater.* **2021**, *43*, 293.
[34] S. Chu, M. Yu, B. Liu, T. Lu, Z. Hou, Y. Qu, F. Zeng, *Chem. Eng. J.* **2022**, *435*, 135188.
[35] Z. Fan, W. Song, N. Yang, C. Lou, R. Tian, W. Hua, M. Tang, F. Du, *Angew. Chem., Int. Ed.* **2024**, *63*, 202316957.
[36] X. Zhao, Y. Zhao, B. Huang, W. Cai, J. Sui, Z. Yang, H.-E. Wang, *Chem. Eng. J.* **2020**, *382*, 123047.
[37] X. Li, Z. Jin, C. Wang, R. Peng, Y. Zha, J. Cao, Y. Ji, Z. Shao, *Adv. Energy Mater.* **2024**, *14*, 2400319.
[38] J. Zhao, Y. Zhang, X. Chen, G. Sun, X. Yang, Y. Zeng, R. Tian, F. Du, *Adv. Funct. Mater.* **2022**, *32*, 2206531.
[39] Y. Wei, R. Yao, X. Liu, W. Chen, J. Qian, Y. Yin, D. Li, Y. Chen, *Adv. Sci.* **2023**, *10*, 2300271.
[40] W.-C. Lin, Y.-C. Yang, H.-Y. Tuan, *Small* **2023**, *19*, 2300046.
[41] K.-T. Chen, S. Chong, L. Yuan, Y.-C. Yang, H.-Y. Tuan, *Energy Storage Mater.* **2021**, *39*, 239.
[42] C.-Y. Tsai, C.-H. Chang, T.-L. Kao, K.-T. Chen, H.-Y. Tuan, *Chem. Eng. J.* **2021**, *417*, 128552.
[43] Z. Yi, J. Xu, Z. Xu, M. Zhang, Y. He, J. Bao, X. Zhou, *J. Energy Chem.* **2021**, *60*, 241.
[44] Y. Xi, X. Wang, H. Wang, M. Wang, G. Wang, J. Peng, N. Hou, X. Huang, Y. Cao, Z. Yang, D. Liu, X. Pu, G. Cao, R. Duan, W. Li, J. Wang, K. Zhang, K. Xu, J. Zhang, X. Li, *Adv. Funct. Mater.* **2024**, *34*, 2309701.
[45] J. Liu, W. Huang, R. Liu, J. Lang, Y. Li, T. Liu, K. Amine, H. Li, *Adv. Funct. Mater.* **2024**, *34*, 2315437.
[46] M. Yu, F. M. Liu, J. H. Li, J. D. Liu, Y. D. Zhang, F. Y. Cheng, *Adv. Energy Mater.* **2022**, *12*, 2100640.
[47] S. Li, L. C. Wu, H. W. Fu, A. M. Rao, L. M. Cha, J. Zhou, B. A. Lu, *Small Methods* **2023**, *7*.
[48] L. You, X. Wang, Q. Zhang, X. Chi, P. Yang, Y. Hu, P. Li, Q. Hui, L. Fang, L. Gu, B. Xu, J. Wang, *Adv. Funct. Mater.* **2022**, *32*, 2112463.
[49] C.-B. Chang, Y.-R. Lu, H.-Y. Tuan, *Energy Storage Mater.* **2023**, *59*, 102770.
[50] J. Guo, H. Zhao, Z. Yang, L. Wang, A. Wang, J. Zhang, L. Ding, L. Wang, H. Liu, X. Yu, *Adv. Funct. Mater.* **2024**, *34*, 2315714.
[51] Z. Wu, G. Liang, J. Wu, W. K. Pang, F. Yang, L. Chen, B. Johannessen, Z. Guo, *Adv. Energy Mater.* **2021**, *11*, 2100185.
[52] Y.-M. Chang, Y.-C. Wen, T.-Y. Chen, C.-C. Lin, S.-C. Huang, C.-S. Ni, A.-Y. Hou, C.-W. Hu, Y.-F. Liao, C.-H. Kuo, S.-F. Liu, W.-W. Wu, L.-J. Li, H.-Y. Chen, *Adv. Energy Mater.* **2023**, *13*, 2301125.
[53] M. Fehse, A. Darwiche, M. T. Sougrati, E. M. Kelder, A. V. Chadwick, M. Alfredsson, L. Monconduit, L. Stievano, *Chem. Mater.* **2017**, *29*, 10446.
[54] T. Zhang, Z. Mao, X. Shi, J. Jin, B. He, R. Wang, Y. Gong, H. Wang, *Energy Environ. Sci.* **2022**, *15*, 158.
[55] Z. Xu, F. Xie, J. Wang, H. Au, M. Tebyetekerwa, Z. Guo, S. Yang, Y.-S. Hu, M.-M. Titirici, *Adv. Funct. Mater.* **2019**, *29*, 1903895.
[56] S.-F. Ho, H.-Y. Tuan, *Chem. Eng. J.* **2023**, *452*, 139199.
[57] P. Hu, Y. Dong, G. Yang, X. Chao, S. He, H. Zhao, Q. Fu, Y. Lei, *Batteries* **2023**, *9*, 238.
[58] N. Kapuria, S. Imtiaz, A. Sankaran, H. Geaney, T. Kennedy, S. Singh, K. M. Ryan, *Nano Lett.* **2022**, *22*, 10120.
[59] N. Ren, L. Wang, J. Dong, K. Cao, Y. Li, F. Chen, J. Xiao, B. Pan, C. Chen, *Chem. Eng. J.* **2023**, *458*, 141489.
[60] R. Tian, L. Duan, Y. Xu, Y. Man, J. Sun, J. Bao, X. Zhou, *Energy environ. Mater.* **2023**, *6*, 12617.
[61] T. Yuan, J. Yan, Q. Zhang, Y. Su, S. Xie, B. Lu, J. Huang, X. Ouyang, *ACS Nano* **2023**, *17*, 10462.
[62] Z. Cheng, B. Zhao, Y.-J. Guo, L. Yu, B. Yuan, W. Hua, Y.-X. Yin, S. Xu, B. Xiao, X. Han, P.-F. Wang, Y.-G. Guo, *Adv. Energy Mater.* **2022**, *12*, 2103461.
[63] W. Yao, C. Tian, C. Yang, J. Xu, Y. Meng, I. Manke, N. Chen, Z. Wu, L. Zhan, Y. Wang, R. Chen, *Adv. Mater.* **2022**, *34*, 2106370.
[64] J. Shao, J. Zheng, L. Qin, S. Zhang, Y. Ren, Y. Wu, *Angew. Chem., Int. Ed.* **2022**, *61*, 202200606.
[65] J.-Z. Yen, C.-B. Chang, K.-S. Jhang, H.-Y. Tuan, *ACS Appl. Energy Mater.* **2023**, *6*, 822.
[66] Y.-J. Liao, W.-W. Shen, C.-B. Chang, H.-Y. Tuan, *Chem. Eng. J.* **2023**, *469*, 143942.